Title: COEXIST: Coordinated single-cell integration of serial multiplexed tissue images

Authors: Robert T. Heussner[1]*, Cameron F. Watson[1,3]*, Christopher Z. Eddy[2], Kunlun Wang[1], Eric M. Cramer[1], Allison L. Creason[1,3], Gordon B. Mills[3], Young Hwan Chang[1,3]

Affiliation:

1. Department of Biomedical Engineering and Computational Biology Program, Oregon Health & Science University (OHSU), Portland, OR, USA
2. Cancer Early Detection Advanced Research (CEDAR), Knight Cancer Institute, OHSU, Portland, OR, USA
3. Knight Cancer Institute, Oregon Health & Science University, Portland, OR, USA

* indicates equal contribution

Corresponding author:
Young Hwan Chang, PhD
Associate Professor
Department of Biomedical Engineering and Computational Biology Program
Knight Cancer Institute
Oregon Health and Science University
Portland, Oregon
Email: chanyo@ohsu.edu

ABSTRACT

Multiplexed tissue imaging (MTI) and other spatial profiling technologies commonly utilize serial tissue sectioning to comprehensively profile samples by imaging each section with unique biomarker panels or assays. The dependence on serial sections is attributed to technological limitations of MTI panel size or incompatible multi-assay protocols. Although image registration can align serially sectioned MTIs, integration at the single-cell level poses a challenge due to inherent biological heterogeneity. Existing computational methods overlook both cell population heterogeneity across modalities and spatial information, which are critical for effectively completing this task. To address this problem, we first use Monte-Carlo simulations to estimate the overlap between serial 5μm-thick sections. We then introduce COEXIST, a novel algorithm that synergistically combines shared molecular profiles with spatial information to seamlessly integrate serial sections at the single-cell level. We demonstrate COEXIST necessity and performance across several applications. These include combining MTI panels for improved spatial single-cell profiling, rectification of miscalled cell phenotypes using a single MTI panel, and the comparison of MTI platforms at single-cell resolution. COEXIST not only elevates MTI platform validation but also overcomes the constraints of MTI's panel size and the limitation of full nuclei on a single slide, capturing more intact nuclei in consecutive sections and thus enabling deeper profiling of cell lineages and functional states.

INTRODUCTION

Multiplexed tissue imaging (MTI) provides spatially resolved molecular profiling of single cells in thin tissue sections[1]. Validating MTI platforms and panels is essential for reproducibility[2], and is often achieved by comparing their performances on serial tissue sections. This comparison assumes uniformity across the sections and is conducted either at the pixel level by marker intensity or at the population level by cell phenotyping[3–6]. However, tissue sections are inherently heterogeneous, driven by factors including the sectioning process, the complexity of the tissue structure, or the presence of rare cell populations[7–10]. A recent study applying cyclic immunofluorescence imaging (CyCIF) to 40μm-thick melanoma sections found more than 90% of the nuclei were not fully intact within 5μm subsections[11]. This finding challenges the prevailing homogeneity assumption in bulk-level cell populations across serial sections. Another study of 4μm thick histological tissue sections showed their mean pixel-wise Pearson correlation was less than 0.6, underscoring their biological heterogeneity[12]. Moreover, fundamental challenges like spectral overlap and tissue degradation limit MTI panels to 40-100 proteins per sample[1]. By contrast, non-spatial technologies like CITE-seq and scRNA-seq can measure over 200 epitopes[13] and 1000 unique molecular identifiers[14] per cell, respectively. Although applying different MTI panels or spatial assays on serial sections allows for deeper molecular profiling, it sacrifices paired single-cell measurements. A computational approach to harmonize these datasets at the single-cell level would mitigate the challenge of unpaired single-cell measurements, improve rigorous validation of MTI technologies, and overcome MTI's panel size limitations[15–17].

While image registration can align serial MTIs by identifying shared landmarks[18–21], achieving perfect alignment at the single-cell level is impossible due to inherent biological variation (**Figure 1A**). These types of approaches either require exceptionally thin sections, do not incorporate the full molecular profiles of the cells, or do not perform unified single-cell level analysis[8,19,21,22].

Furthermore, our previous work reported natural variations between serial sections in the image-to-image translation task, especially when using consecutive H&E sections to infer immunofluorescence intensity[18,20]. Recent platforms such as RareCyte Orion[16] or studies[23] are prioritizing multimodal assays such as CyCIF and hematoxylin and eosin (H&E) or high-plex protein combined with whole transcriptome sequencing in the same section to address this problem. Beyond MTI, many spatially resolved single-cell assays utilize serial tissue sections due to technological constraints[15], including Nanostring CosMX[24], spatial proteogenomics[25], and others[26].

Computational multi-omic integration methods aim to pair single-cell datasets and can be extended to spatial assays[27]. These methods assume similar cell states across datasets and use techniques such as canonical correlation analysis (CCA)[28] or variational autoencoders[29] to jointly embed single-cell representations and match them across modalities[30]. Linear sum assignment (LSA)[31,32] is frequently used as a framework to achieve this matching by constructing a cost matrix of potential cell pairs and identifying a set of pairs of minimal overall cost[33,34]. For example, MaxFuse[35], a recent approach backboned by LSA, is specifically designed for weakly linked modalities with few shared features, including proteomic, transcriptomic, and epigenomic information at single-cell resolution on the same tissue section. It generates nearest-neighbor graphs, identifies anchor cells based on linked feature correlation, and then iteratively refines matches with graph smoothing and CCA. However, current multi-omic integration strategies are not compatible with spatial assays, as they fail to include spatial information and incorrectly assume homogeneity within the population, particularly when dealing with serial sections. Alternatively, cell tracking algorithms[36], designed to track cell movements across video frames, can be adapted to treat serial images as sequential frames but do not leverage the rich molecular profiles provided by MTI. Therefore, it is essential to develop a single-cell integration method that

combines molecular characteristics with spatial context to effectively integrate multi-modal or multi-panel datasets obtained from serial tissue sections.

To address this, we first design a Monte-Carlo simulation to estimate the theoretical overlap of single cells across consecutive tissue sections (**Figure 1B**). We then examine how LSA can be used with cell tracking algorithms, highlighting the importance of an approach based on tracking. Next, we introduce COEXIST, which leverages spatial information and shared biomarker expression to pair individual cells across consecutive tissue sections (**Figure 1C**). We apply our method to the Human Tumor Atlas Network (HTAN) Trans-Network Project tissue microarray (TNP-TMA) breast cancer (BC) dataset, where we phenotype cells using a combined tumor and immune panel of 42 unique molecular features, nearly doubling the number of features compared to a single panel. Our algorithm allows for the full reconstruction and characterization of 2.5D tissue, making it highly versatile for integrating spatial multi-omics data to analyze emerging spatial assays[37].

RESULTS

Challenges in spatial profiling across serial sections

Our Monte-Carlo simulation (**Methods**) indicates that approximately 62% of cells are shared across consecutive sections in the TNP-TMA BC dataset, which employs 5μm-thick sections and has a mean nuclear diameter of 7.8μm (with a standard deviation of 2.4). We assumed nuclei to be spheres with normally distributed diameters to simplify the simulations based on the nuclear size statistics extracted from each image. While the purpose of the simulation was to provide a rough estimate of the fraction of nuclei shared across consecutive sections, it aligned with recent literature[11] and closely matched results from the cell tracking algorithm. Additionally, we repeated the simulation using the nuclear size statistics and section thickness from another study of 3D tissue CyCIF[11]. Our simulation yielded comparable results to the ground-truth measurements:

89.3% of nuclei were not fully intact in 5μm thick sections (compared to >90%)[11], while 71.3-77.6% remained fully intact within 30-40μm sections (compared to 60-80%)[11]. Thus, our simulation provides a reliable estimate for the fraction of cells shared across serial sections. The level of cell colocalization between serial sections varies significantly based on section thickness and cell size (**Figure 1B**) where each bar represents a different TMA core. These results motivate a new approach to allow rigorous validation and integration of serial sections at the single-cell level.

Improved integration using cell tracking over linear sum assignment (LSA)

Many multi-omics integration methods operate with the assumption that cell populations are shared across serial sections, allowing for the matching of populations by linking cells within the same molecular states. However, our simulation revealed applying this assumption directly to spatial assays and solely focusing on optimizing linked molecular feature correlation via LSA does not guarantee spatial coherence of the matches (**Figure S1A**). Alternatively, adopting cell tracking algorithms that rely on cell morphology and location for this problem can guarantee spatial coherence[36] (**Figure S1B**). In our subsequent analysis, we investigate the use of both approaches for the integration problem and propose a novel algorithm that overcomes their respective limitations. We frame the problem as finding a single-cell matching between a reference and target image, representing consecutive MTIs. We define match quality as the mean Spearman correlation of the shared molecular features of the paired cells.

LSA achieves higher match quality compared to cell tracking given the same reference cells. This is because LSA directly optimizes shared feature correlation, whereas cell tracking does not, and considers matches across arbitrary distances, while cell tracking cannot (**Figure S1A**). Therefore, to implement LSA we introduced spatial constraints to the Jonker-Volgenant (JV) [38] algorithm to restrict potential matchings to a local neighborhood of size *r*. This modification also mitigates local registration discrepancies, overcoming possible failures in image registration. To create a fair

benchmark for LSA and cell tracking, we first identified *N* anchor cells from a reference MTI that comprised *M* (*M* > *N*) cells using the cell tracking algorithm. This ensured that the benchmark reference cells were associated with spatially coherent target candidates (**Methods**). We then used our spatially constrained LSA implementation to identify target matches for the *N* anchors, iteratively expanding the radius parameter. Additionally, we conducted LSA by randomly sampling *N* anchor cells from the reference slide to test the importance of cell tracking in choosing suitable anchor cells instead of using random anchor cells. We then repeated the radial expansion process to create sets of matches.

Within neighborhoods smaller than 50μm, or approximately 6 nuclei, where the true pairs are expected to reside, we observed higher quality matches for the *N*-tracked anchors than the *N*-randomly selected anchors (**Figure 2A**). Therefore, cell tracking is an essential precursor for attaining matches that are both high in quality and spatially coherent. However, when extending this process to all *M (>N)* reference cells, the resulting matches exhibit lower quality due to *M* exceeding *N*. This trend remains consistent across other cores (**Figure S2**). As we know only a fraction of *M* is physically shared across sections, applying LSA without anchors is not ideal. To illustrate the bulk-level matching without considering spatial information, we employ LSA without using anchors or neighborhood constraints. Interestingly, match quality slightly surpasses this bulk-level correlation at neighborhoods larger than 200μm in the previous unanchored neighborhood expansion scenario (**Figure 2A**). This occurs because LSA optimizes linked feature correlation at the individual cell pair level, whereas we assess match quality at the matched population level. While the sum of costs is lower in the bulk-level case, suggesting potentially higher-quality individual matches, it does not translate to higher overall match quality as we measure it.

We also explored the robustness of spatially constrained LSA by measuring its cycle consistency[39], which assesses the algorithm's ability to maintain consistency in assigning matches when swapping the order of the reference and target MTIs. To do this, we matched the original *N*-tracked reference cells with all potential target cells. Then we did the opposite by matching the original *N*-tracked target cells with all potential reference cells. We measured cycle consistency by calculating the fraction of shared matches between both sets relative to *N* (**Figure 2B**). Our findings revealed a rapid decrease in cycle consistency beyond 5μm neighborhoods, dropping to below 50% at 10μm. This underscores that LSA, widely used as the framework for multimodal integration[35], can yield unstable results depending on the order of reference and target MTIs and the number of cells present in the target MTI. In contrast, tracking-based algorithms ensure cycle consistency.

COEXIST

While LSA generates quality matches, empirically fine-tuning neighborhood size is still challenging and subjective. Cell tracking is better suited for this problem because it directly leverages spatial and morphological information and does not require a radius parameter. However, cell tracking does not account for molecular information and is susceptible to erroneously matching cells that overlap but are merely adjacent in the lateral dimension. Therefore, we introduce COEXIST (**Methods**), which combines cell tracking with the molecular feature distance metric used in LSA. By integrating spatial, morphological, and shared feature information, COEXIST provides a robust framework for improving matching accuracy. As we demonstrated the weakness of LSA, we benchmarked COEXIST to the baseline cell tracking algorithm and found it consistently improved the shared feature correlations of the matches, often by more than 5% (**Figure 2C**). Small decreases in shared feature correlation for specific markers in some cores occurred due to artifacts or tissue loss in the round the markers were stained and imaged.

Cell type assignment using label propagation and validation

To ensure robust validation of our approach, we use full panel data and synthetically generated two panels to validate COEXIST for refining cell types and label propagation (**Methods**). In this setup, the cell types identified in the full panel serve as the ground truth, enabling us to assess how many anchors are required and evaluate the effectiveness of label propagation (**Figure 3A**). This experiment was designed to simulate realistic experimental constraints, where only a fraction of cells can be consistently tracked across consecutive slides, and a reduced subset of markers (50% shared markers in the case of the TMA dataset) is available for k-NN propagation. We tested cell-type label propagation by synthetically generating sub-panels with a random selection of half of the biomarker from the full dataset, simulating the necessity of propagating labels using overlapping markers to untracked cells on consecutive sections.

The experiment was performed on two datasets: (1) a region of interest (ROI) from a healthy tonsil specimen (~70,000 cells) (**Figure 3B**), and (2) a whole-slide image (WSI) of colorectal cancer (CRC) tissue with adjacent normal tissue (~480,000 cells) (**Figure 3C**). Results showed that as the proportion of tracked cells increased towards the theoretical maximum of 100% tracking across consecutive sections, label propagation performance, measured by F1 score, improved for both the tonsil ROI and CRC WSI datasets (**Figure 3D**). For k-NN propagation across 1000 random panels with 60% cell tracking, the mean F1 scores were 0.78 (SD 0.04) and 0.76 (SD 0.03) for the tonsil ROI and CRC WSI datasets, respectively. These scores approached the maximum theoretical mean F1 scores of 0.82 (SD 0.03) and 0.81 (SD 0.02). Importantly, this trend was consistent across varying anchor cell proportions, despite high variations between panels within each anchor cell proportion. Furthermore, both highly performing and poorly performing panels improved as the anchor proportion increased (**Figure 3E**). These findings highlight that in addition to the proportion of cells tracked across consecutive sections, the specific

biomarker composition of the sub-panels plays a critical role in label propagation performance. This underscores the importance of carefully selecting markers to maximize the accuracy and reliability of cell-type assignments across tissue sections.

COEXIST enhances spatial single-cell profiling

We performed a comprehensive analysis of all BC TMA cores, using combined tumor and immune CyCIF panels with a total of 42 unique biomarkers (**Table S1**). We observed several discrepancies in the uni-panel phenotypes compared to the combined panel (**Figure 4A**). Specifically, cells profiled with the immune panel showed a predominant immune cell population, whereas the tumor panel did not exhibit such dominance. However, the combined panel revealed a more balanced population between these two cases, highlighting COEXIST's ability to refine phenotypes. BC subtype-specific differences contribute to certain batch effects, making an integrative analysis challenging without rigorous normalization[40]. Nevertheless, high-level phenotyping showed evident biases towards the dominant cell population being profiled for a given panel, (i.e. immune or tumor cells), which COEXIST effectively corrects.

We then conducted a thorough phenotypic analysis focusing on triple-negative BC (TNBC) core E6 with combined tumor and immune CyCIF panels comprising 42 biomarkers (**Table S1**). We identified 13 distinct cellular phenotypes, unveiling spatial heterogeneity at an unprecedented level (**Figure 4B** and **4C**). However, clustering cells based solely on either the immune or tumor panels failed to capture their full phenotypic diversity (**Figure 4B**). For instance, the immune panel lacked markers such as CK14, CK17, PCNA, CD31, and Vimentin, which restricted its ability to delineate different epithelial sub-states, vasculature, or cells that may be undergoing Epithelial-to-Mesenchymal transition. Meanwhile, the tumor panel could not differentiate between CD8+ or CD4+ T-cells and lacked markers entirely for B-cells and all myeloid lineage cells including macrophages and monocytes. The combined panel rectified these shortcomings and even

revealed a distinct stroma cell population. Shared markers across the panels clustered closely (**Figure 4C**) with moderate Spearman correlations (**Figure S3**).

To further investigate cell identity switching, we examined a population of 138 cells that were classified as αSMA+ stromal cells in the tumor panel but reclassified as macrophages when the immune panel was incorporated (**Figure 4D**). For this population of cells, lineage marker intensities were ranked against the remaining cells in the core using each panel. In the tumor panel, αSMA and Vimentin emerged as the highest-ranked markers. Meanwhile, in the immune panel, markers such as CD14, MHC II, CD11b, αSMA, CD45, CD163, and CD68 were among the most prominently ranked, driving the identification of the macrophage population. On the combined panel (depicted in purple for markers originating from the tumor panel and green for those from the immune panel in **Figure 4D**), CD14 and MHCII were notably more differentially abundant compared to αSMA. These differences likely stem from the absence of myeloid-specific lineage markers in the tumor panel. Without these lineage-specific markers, fluorescent spillover from nearby cells or high autofluorescence in other channels makes the misclassification of cell types more likely (**Figure S4**). The integration of both panels effectively resolved this discrepancy. Apart from these markers, profiles across the cells were generally similar.

Next, we propagated the rich phenotype labels to the unshared cells in each section using k-Nearest Neighbors (k-NN) (see **Methods**), showing increases in cell type diversity for each panel (**Figure 4E**). The immune panel inherits increased cell type resolution within the epithelial and stromal compartments, while the tumor panel shows a large expansion in immune cell type resolution. The resulting spatial distribution of cell types in the two sections appeared very similar after label propagation (**Figure 4E**). To quantify this similarity, we determined the cell type composition of all cells utilizing k-NN propagation (**Methods**). The propagated cell composition remained consistent across panels when compared to their original counterparts (**Figure S5**). We

also documented recurrent cellular neighborhoods around cells shared by the two panels. Our recurrent neighborhood (RCN) analysis showed consecutive sections varied in the abundance of certain neighborhoods, such as RCN 3, 4, 5, and 8 (**Figure 4F**). This highlights the weakness in assuming spatial homogeneity across the tissue block. Other neighborhoods are similarly abundant across the two panels. One such neighborhood, RCN 7, is composed primarily of CD163+ Macrophages, CD31+ Endothelial cells, and CD20+ B-cells (**Figure 4G**). These lineage markers are spread across the two panels, and therefore the co-localization of these cell types would have been missed without the combination of the two panels. This RCN may suggest that vascular regions play an important role in immune cell infiltration. Further, this example highlights the utility of panel combination to uncover potentially biologically meaningful functional tissue units.

COEXIST elevates cross-MTI platform validation

Validating across MTI platforms is critical for ensuring scientific reproducibility in spatial biology. We demonstrated COEXIST's effectiveness in comparing MTI platforms using serial sections from normal jejunum core B4 in the TNP-TMA BC dataset processed with CyCIF and multiplex immunohistochemistry (mIHC)[17]. We compared the section bulk-level population compositions and found a strong Pearson correlation (r = 0.8) between the platforms (**Figure 5A**). This result is expected and has been demonstrated by other groups[4]. We performed the population comparison exclusively on the subset of shared cells identified by COEXIST, observing a similar correlation (r = 0.85) in compositions (**Figure 5B**). However, recognizing the limitation of bulk-level comparisons, we assessed the platforms at the single-cell level and found a moderate correlation, with Spearman correlations ranging from 0.26 (CD11B) to 0.81 (PanCK) (**Figure 5C**). The lower Spearman correlations observed at the single-cell level compared to the population level can be attributed to the limited presence of positive populations for certain markers (i.e. rare cell types). Additionally, we noticed the impact of the nonlinearity introduced by the IHC enzyme reaction, which affects the signal's conversion to expression levels.

DISCUSSION

While staining a single tissue with both panels would be ideal, it is often impractical due to tissue loss and signal degradation caused by multiple rounds of CyCIF. To address this, our method introduces an innovative cell tracking and propagation framework that integrates complementary antibody panels across sections. This approach expands the phenotypic space without requiring all markers to be present in a single section. Building on this, we recognize that prevalent multi-omic integration methods often do not pair the same cells across modalities; instead, they rely on matching cells with similar molecular states using limited shared information. However, our study highlights that characterizing molecular states based solely on shared marker information for matching is not sufficient to capture the true spatial relationships between cells, and further, spatial information is crucial for precise single-cell matching.

To combat this challenge, we developed COEXIST and demonstrated its utility for precise single-cell matching across serial sections. Using COEXIST, we could resolve differences between two orthogonal MTI panels with limited marker overlap and establish a set of refined cellular phenotypes on breast cancer tissues from a Human Tumor Atlas Trans-Network Project (TNP) Tissue Microarray. Further, we successfully establish highly resolved cell phenotypes for one triple negative breast cancer core. While individual panels can cause misclassification of some cell populations across serial sections, due to the absence of key lineage markers, COEXIST rectified these discrepancies. Our neighborhood analysis revealed unique and potentially biologically significant spatial structures, such as a neighborhood enriched for vascular cells and a diverse complement of immune cells, that could be captured only by the combined panel. Additionally, COEXIST mitigated the problem of overcalling specific lineages that is common in panels designed for specific cell types like immune cells, fibroblasts, macrophages, and malignant epithelial cells, thereby contributing to more accurate cellular phenotyping across diverse tissues.

We show the COEXIST algorithm has *O(n)* time complexity with respect to the number of input cells, making it highly scalable to large MTIs (**Figure S6**). However, the preprocessing step of computing the pairwise correlation distances is $O(n^2)$, which can be improved by only computing local distances rather than all possible distances. It is important to note employing COEXIST necessitates the use of two consecutive slides, which should be considered in the context of experimental design and cost management. Mitigating the cost challenge, analysis of two consecutive slides overcomes the problem that 90% of nuclei not being fully intact within 5μm sections[11] with about 60% of the nuclei being intact across two 5μm sections. COEXIST's key assumption is that the shared cell population is representative of the broader tissue population. However, this assumption may not hold in cases where the tissue sections are thicker than the average cell diameter, potentially leading to a disproportionate representation of certain cell populations. In this study, we focused on two consecutive sections; however, this approach can be expanded. For example, with three consecutive slides, we anticipate a reduced overlap in cell populations across the three sections. Nonetheless, we can analyze two consecutive sections simultaneously by treating the middle section as our reference and then using the two consecutive sections for COEXIST analysis. Interestingly, the matched cells generated by COEXIST show only moderate shared feature correlations, which is unexpected considering the direct linkage of protein marker expression through tissue processing and antibodies. This contrasts with multi-omics, where the linkage between features is weaker. Studies exploring differences in paired multi-omics measurements often reveal discrepancies[41,42]. Several factors contribute to these observed single-cell discrepancies; First, many shared markers identify rare cell populations, leading to most cells being "negative" (**Figure 5C**). Second, compartment-level differences are not accounted for. For example, the immune cells, which tend to be significantly smaller than malignant cells, could be especially affected depending on how the section is cut in a 2.5-dimension. Third, technical batch effects are expected between MTI platforms, for instance, mIHC

uses enzymatic labels for molecule tagging, whereas CyCIF employs immunofluorescent labels[43]. Comparatively, CyCIF-CyCIF integration exhibits stronger linear relationships in the expression levels of shared markers (**Figure S7**). These factors should be considered in future multi-omics integration studies.

In addition to requiring two consecutive sections, COEXIST assumes that spatial proximity and shared marker expression serve as reliable anchors for matching. However, we do not impose strict assumptions about the distribution of cell features or spatial organization, acknowledging that these characteristics can vary widely across tissue types. Despite this flexibility, we recognize that these assumptions may introduce biases, particularly in complex tissues with highly heterogeneous cell distributions. Publicly available datasets suitable for validating COEXIST across diverse tissue types remain sparse. To address this, we experimented using two single-slide datasets: one from a healthy tonsil specimen and another from a colorectal cancer (CRC) tissue sample. These datasets were used to validate the propagation of cell type labels under varying degrees of cell tracking efficiency and across random biomarker panels. The two tissue types represent very different spatial organizations — tonsil tissue is highly spatially stratified by cell type, while CRC tissue is more spatially mixed. Notably, both tissue types showed improved label propagation performance as cell tracking efficiency increased. To establish an upper bound for label propagation performance, we simulated perfect cell tracking by using 100% of cells for k-NN training. In this scenario, label propagation errors could only be attributed to missing key biomarkers in reduced panels or shared markers across consecutive sections. This finding highlights the importance of marker selection, especially for future multimodal applications where feature correspondence across modalities may be limited.

Alternative computational integration methods employ strategies such as dimension reduction or graph smoothing to reduce complexity in high-dimensional data. However, MTI panels are

relatively compact compared to broader single-cell assays and are often designed to measure orthogonal or complement features, such as the tumor and immune panels in the TNP-TMA BC dataset. Therefore, those strategies are not required for our applications in this paper. However, for tasks requiring high-dimensional multimodal integration, COEXIST is highly compatible with joint embedding approaches[29,35], as the embeddings can be interchanged with linked molecular profiles, making COEXIST adaptable to a wide range of spatially resolved datasets. COEXIST is designed to allow researchers to fully leverage MTI technologies and improve MTI assay development. It has the potential to be applied to any spatially resolved assays, such as protein and RNA for multimodal integration.

METHODS

Preprocessing

The TMA dearray[44], illumination correction, and tile alignment and stitching were conducted within the Galaxy-MCMICRO Environment[5]. The cells and nuclei were segmented using common nuclear (DAPI) and membrane markers (Pan-cytokeratin, CD45) with Mesmer[45]. Corresponding cells and nuclei were assigned the same label, and cells without a corresponding nucleus were removed. Consecutive nuclear masks were registered using MATLAB's imregister function[46]. The nuclei pixel coordinates, centroid, and marker mean intensities were extracted with scikit-image[47].

Quality control

Quality control procedures were implemented to ensure the integrity of the TMA cores. Out of the original 88 TMA cores (3 consecutive tissue sections per core), 49 were removed due to various issues encountered during imaging and processing, including fluorescent artifacts in the images, tissue loss, and registration failures. Notably, the majority of registration failure cases of samples were not consecutive sections, indicating a significant difference in tissue architecture. Since our approach depends on consecutive tissue, we use quality-controlled cores to showcase COEXIST.

Monte-Carlo simulation

To empirically estimate nuclei sharing across consecutive tissue sections, we conducted a Monte-Carlo simulation. Our analysis is based on three main assumptions about the system:

1. The nuclei are spatially uniformly distributed. 2. The nuclei are spherical with normally distributed diameter. 3. Nuclei are present in a section if their boundary overlaps the section boundary.

Algorithm: Monte-Carlo simulation to estimate nuclei sharing across consecutive sections

Input:

I: number of repetitions
M: nuclear diameter mean (μm)
S: nuclear diameter standard deviation (μm)
W: section thickness (μm)
B: minimum and maximum tissue thickness (μm)

Initialize:

n_shared = 0: number of shared nuclei in sections 1 and 2
n_unshared = 0: number of unshared nuclei present in section 1

for *i* from 1 to *I* **do**
    draw nucleus radius *r* from normal distribution parameterized by *M* and *S*
    draw nucleus coordinate *x* from uniform distribution bounded by *B*
    get nucleus bounds n_{min}, $n_{max} = x \pm r$
    if $n_{min} < W < n_{max}$ **then**
        n_shared += 1
    else if $0 < n_{max} < W$ **then**
        n_unshared += 1
    else
        continue
    end if
end for
f_shared = *n_shared* / (*n_shared* + *n_unshared*)
return *f_shared*

Cell tracking

We adopt single-cell tracking using Voronoi partitioning via stable matching[36]. To reduce its computational time, we implement majority voting and cycle consistency within stable matching. Our method is a two-step process: first, we perform a majority vote from the reference slide to the target slide. Then, we ensure cycle consistency by considering the target slide back to the reference, guaranteeing uniqueness in the matching procedure for tracking.

Formally, given sets P and Q, representing nuclei present in serial tissue section images I_P and I_Q, we aim to find P ∩ Q defined as subsets $P \subseteq$ P and $Q \subseteq$ Q such that elements $p_i \in P$ and $q_i \in Q$ represent the same nucleus present in both sections, where n(P) = n(Q). We begin with nuclear

segmentation label masks $M_P \in \mathbb{Z}^{m1 \times n1}$ and $M_Q \in \mathbb{Z}^{m1 \times n1}$. To match a nucleus $p_i \in P$ to nucleus $q_i \in Q$, the tracking algorithm first identifies nuclear region $r_{pi} \in M_P$ representing the pixel coordinates of p_i, ensuring spatially coherent match candidates. Next, nuclei q with regions $r_q \cap r_{pi}$ are considered for matching and nucleus $q_i \in q$ is assigned as the nucleus with the maximum region overlap between p_i and candidates q. To ensure cycle consistency, the reverse process is completed (assigning q_i to candidates p). If the subsequent assignment is not p_i, the nuclei are considered unmatched. In the case where multiple candidates in q have equivalent region overlaps of p_i, the candidate with the minimum centroid distance to p_i is chosen.

Linear sum assignment (LSA)

LSA offers an alternative framing of the problem by finding a linear matching between sets P and Q such that the sum of the match costs is minimized. We begin with cell-feature arrays $F_P \in \mathbb{Z}^{m2 \times n2}$ and $F_Q \in \mathbb{Z}^{m3 \times n2}$, where features of F_P and F_Q are the shared molecular features. F_P and F_Q are standardized to a mean of 0 and standard deviation of 1 to remove intensity range variations. The pairwise Spearman correlation distance, 1 – Spearman's ρ, between nuclear pairs $D \in \mathbb{R}^{m2 \times m3}$ is used as the cost matrix. While Spearman's correlation is a non-parametric similarity measure rather than a strict distance metric, we treat 1−Spearman's ρ as a distance-like measure. This allows positive correlations to correspond to low costs and negative correlations to high costs, aligning with the optimization goal. Spearman's ρ was chosen over Pearson's ρ because it is robust to outliers and measures the strength of monotonic relationships between marker expression profiles. Additionally, in the context of multiplex tissue imaging (MTI), mean intensity

feature correlation is commonly used, which motivated the choice of Spearman correlation over alternatives such as cosine distance. However, we acknowledge the potential benefits of cosine distance and may explore it in future work.

A limitation of this approach is that it does not guarantee matches p_i, $q_i \in P$, Q are spatially coherent. To address this, we incorporate spatial information by modifying D before applying LSA by assigning infinite cost to nuclear pairs that have intercellular distances greater than an empirically determined radius using the pairwise x-y projection of the Euclidean centroid distance $E \in \mathbb{R}^{m2 \times m3}$. The SciPy implementation[47] of the modified Jonker-Volgenant algorithm[38] was used for this purpose, which extends the JV algorithm to the rectangular assignment problem where the bipartite graph has an unequal number of nodes in each class. This modification is necessary because there are often unequal numbers of cells across modalities/tissue sections. This algorithm is compatible with any cost matrix representing the “cost” of assigning nodes from different classes to each other. Costs can be positive, negative, or zero, and the goal of the algorithm is to find a 1:1 matching such that the sum of the overall costs is minimized.

COEXIST

We propose COEXIST for integrating serial MTI slides of reasonable thickness. This algorithm combines spatial and biomarker expression information to match single cells present in both slides. We use D as described previously in place of the distance measure (region overlap or centroid distance) in the cell tracking algorithm. Therefore, spatially coherent candidate cells are considered, but matches are assigned by shared molecular profiles. In scenarios where there exists no molecular linkage F_P and F_Q, cell tracking can be used.

Clustering and label propagation

After identifying the shared subpopulation, we cluster the cells with GPU-accelerated Phenograph[40] and propagate the labels to the remaining cells in each slide. Clustering parameters *n_neighbors* were set to 60, 70, and 100 for the tumor panel, immune panel, and shared subpopulation, respectively, and *min_size* was set to 100 for all. For all clustering performed in our analyses, we explored a range of different clustering granularities in order to find the resolution that generated clusters for which we were able to reliably annotate as biologically meaningful cell types. To achieve label propagation to the unshared subpopulation of each section, we fit a GPU-accelerated k-Nearest Neighbors (k-NN) classifier from the RAPIDS library[48] on the panel-specific markers of the shared subpopulation along with their phenotype labels. For each cell of the unshared subpopulation, we use the panel-specific k-NN classifier to query and majority-assign the superplexed labels of its 10 nearest neighbors in the shared subpopulation, determined using the default Euclidean distance.

Validation of cell-type label propagation

For both the tonsil ROI and CRC WSI datasets, quantified cellular feature tables were downloaded from publicly available repositories. Each dataset included 24 relevant protein markers after excluding DAPI and autofluorescence channels. Marker intensities were log1p transformed, and a standard scaler was applied using Scanpy. Subsequently, Scanpy was used to generate a neighborhood graph, compute a UMAP representation, and perform Leiden clustering on each dataset separately. The resolutions used for Leiden clustering were determined empirically, with a value of 0.5 identified as optimal for capturing biologically meaningful cell types in both datasets. This resulted in 13 cell types for the tonsil ROI and 17 cell types for CRC WSI datasets. The resulting Leiden cluster labels, prefixed with “T” for the Tonsil ROI dataset and “C” for the CRC WSI dataset, were used as ground-truth labels for the following experiments.

To simulate tracking variability, we generated 1,000 random panels, each containing 12 markers selected from the original set of 24 markers. The cell feature tables were then divided into 'tracked' and 'untracked' matrices across a range of proportions, from 10% to 100%. This range represents varying levels of tracking efficiency, with 10% corresponding to poor tracking and 100% representing perfect tracking. Based on our data, a realistic expectation for tracking efficiency is approximately 60% of cells shared between consecutive tissue sections.

The 50% reduction in panel size reflects practical limitations in shared marker availability, simulating the realistic training data size for k-nearest neighbors (k-NN) label propagation to untracked cells. This setup mirrors scenarios encountered in TMA data, where 48 markers are used for cell phenotyping and 24 markers are available for k-NN per panel. Consequently, targeting 50% marker usage for our simulations reflects real-world constraints on shared biomarker panels.

For each anchor cell proportion and random panel, a k-NN classifier was trained on the 'tracked' matrix using only the intensities of the 12 random markers and the ground-truth Leiden cluster annotations as training labels (**Figure 3A**). To ensure consistency across anchor cell proportions and emphasize local cell relationships, the number of neighbors (*n*_neighbors) was set to 10 for all cases. The trained classifier was then used to predict Leiden cluster labels for cells in the 'untracked' matrix. To evaluate performance, a subset of predicted labels (5,000 cells for the tonsil ROI and 40,000 cells for the CRC WSI dataset) was sampled and compared to the ground-truth annotations to compute an F1 score. F1 scores were calculated as a weighted average across Leiden cluster labels for each random panel. For the 100% tracked scenarios, a random sample of the tracked cells was used for both prediction and scoring to establish a theoretical maximum performance benchmark.

Cell phenotyping

The Phenograph-derived clusters were used to assign broad cell types across all breast cancer and normal breast tissue cores that passed quality control; however, this combined clustering lacked sufficient resolution to classify cell types beyond high-level lineages (Epithelial, Immune, Stroma, etc.). To conduct more detailed analyses, one triple-negative breast cancer core from the TMA (E6) was selected and subjected to independent cell phenotyping. For individual core phenotyping, Scanpy[49] was used to cluster cells based on a subset of lineage-specific markers from the tumor, immune, and combined panels. A neighborhood graph was constructed using default parameters (*scanpy.pp.neighbors*), and clusters were assigned using Leiden clustering (*sc.tl.leiden*), with the *resolution* parameter set to 2. Leiden clusters were annotated and binned into cell types based on the mean intensities of lineage markers for each of the three panels. Propagation of core-specific labels from the combined panel to the unshared population of each panel was conducted in the same manner as described in the previous section. To characterize a subpopulation of cells that switched identities between panels, lineage markers were ranked (*scanpy.tl.rank_genes_groups*) for the subpopulation against the remaining cells in the core for each panel.

Recurrent neighborhood analysis

For core E6, a Recurrent Cellular Neighborhood (RCN) analysis[50] was conducted to examine the spatial arrangement of cell types between the two panels after label propagation. For each panel, anchor cells for the neighborhood analysis were considered as those that were shared across the panels. For each panel independently, a Scikit-learn[51] KDTree was used to calculate a counts matrix of neighboring cell types within 30μm of anchor cells. The neighborhood counts were converted to proportions, and these relative neighborhood matrices from the two panels were concatenated together. Neighborhoods were clustered using K-means clustering into 15 unique

RCNs. Values in the range of 5-50 were used to construct an elbow plot to determine the final number of clusters for the k-means clustering.

Data visualization

The *ggplot2*[52] and *ggAlluvial*[53] packages were used to generate stacked bar plots and alluvial diagrams in R[54]. All other plots were generated using the seaborn[55] and matplotlib[56] packages in Python. Visualizations of the actual multiplex tissue images were captured using Vitessce[57,58] within the Galaxy-MCMICRO Environment[5].

Statistics and Reproducibility

We utilize both Pearson and Spearman correlation analyses in our study to explore variable relationships. Pearson correlation assesses linear connections among continuous variables, while Spearman correlation evaluates monotonic relationships, which may not be strictly linear.

To guarantee result reproducibility, we provide all the necessary code snippets and scripts used in our analysis. This includes data processing steps, statistical analyses, and visualization methods.

Data Availability

As part of this paper all images at full resolution, all derived image data (e.g. segmentation masks), and all cell count tables will be publicly released via the NCI-recognized repository for Human Tumor Atlas Network (HTAN; https://humantumoratlas.org/) at Sage Synapse (associated Identifiers: HTAN TNP – TMA, OHSU_TMA1_004-XX) where XX represents TMA core ID. The tonsil image dataset used for the label propagation experiment is available at https://www.synapse.org/MCMICRO_images and will be made available through the Human

Tumor Atlas Network. The CRC WSI dataset is available through the Human Tumor Atlas Network (associated identifiers: HTAN TNP – SARDANA, HTA13_1_6).

Code Availability

All software used in this manuscript is detailed in the article's Methods section and its Supplemental Information. The associated scripts are freely available via GitHub as described at https://github.com/heussner/coexist.

Acknowledgments

This work was carried out with major support from National Cancer Institute (NCI) Human Tumor Atlas Network (HTAN) Research Centers at OHSU (U2CCA233280). Y.H.C is supported by R01 CA253860, U01 294548 and Kuni Foundation Imagination Grants. The resources of the Exacloud high-performance computing environment developed jointly by OHSU and Intel and the technical support of the OHSU Advanced Computing Center are gratefully acknowledged.

Author Contributions

Conceptual development: R.T.H., G.B.M, Y.H.C. Data analysis and computational implementation: R.T.H, C.W, C.Z.E., Quality control (QC) of raw data: K.W, E.C. Manuscript writing: R.T.H, C.W, C.Z.E, A.L.C., Y.H.C. All authors contributed to the paper either through discussions or directly.

Declaration of interests

The authors declare the following competing interests: G.B.M. is a SAB member or Consultant: for Amphista, Astex, AstraZeneca, BlueDot, Chrysallis Biotechnology, Ellipses Pharma, GSK, ImmunoMET, Infinity, Ionis, Leapfrog Bio, Lilly, Medacorp, Nanostring, Nuvectis, PDX Pharmaceuticals, Qureator, Roche, Signalchem Lifesciences, Tarveda, Turbine, Zentalis

Pharmaceuticals. G.B.M. has Stock/Options/Financial relationships with: Bluedot, Catena Pharmaceuticals, ImmunoMet, Nuvectis, SignalChem, Tarveda, and Turbine. G.B.M. has Licensed Technology: HRD assay to Myriad Genetics, DSP patents with Nanostring. G.B.M. has Sponsored research with AstraZeneca. The other authors declare no competing interests.

FIGURES

Figure 1: COEXIST integrates serial multiplexed tissue images. (A) Visualization of shared (green) and unshared (yellow/blue) cells across serial tissue sections. **(B)** Monte-Carlo simulation estimates approximately 62% of cells are present in serial sections. **(C)** Overview of single-cell integration and downstream analysis: Cell-feature tables of serial tissue sections with shared and unshared features are integrated with an algorithm that accounts for the spatial and protein expression information, identifying the shared (green) and unshared (yellow, blue) cell populations. The shared cells undergo phenotyping using the combined panel, with resulting cell type labels being extended to the remaining unshared cells for each section. This propagation of cell type labels to the unshared cells is achieved via K-Nearest Neighbors.

Figure 2: Cell tracking improves integration quality over linear sum assignment. (A) Tracked anchors outperform random anchors in reasonably sized neighborhoods. Error bars indicate the standard deviation of five seeds with the constrained case representing bulk-level or LSA without spatial constraint. **(B)** Cycle consistency of LSA rapidly diminishes with increasing neighborhood size, whereas cell tracking ensures cycle consistency. **(C)** Heatmap showing the match correlation percent improvement when enriching the tracking algorithm with protein expression information for each TMA core and shared feature, with eight shared markers serving as ground truth for matching and integration. These markers are present in consecutive tissue sections within the dataset.

Figure 3: Label propagation is robust to biomarker panel composition, tracking efficiency, and tissue type (**A**) Overview of single-slide validation experiment. Ground-truth cell type clusters were generated on all cells and all biomarkers for a tissue section dataset. Across a range of proportions, the cells were split into ‘tracked’ (green) and ‘untracked’ (yellow) matrices. Within each tracking proportion, the matrices were subset to a random biomarker panel half the size of

the original panel. A K-NN classifier was trained on the 'tracked' cells and used to predict which ground-truth clusters an 'untracked' cell belonged to. The predictions were randomly subsampled and compared against the ground-truth labels from the 'untracked' cells. (**B**) Ground-truth Leiden clusters (n=13) for a healthy tonsil dataset. Cells are annotated by Leiden cluster in a 2D UMAP representation of the full biomarker panel (left) and a spatial scatterplot (right). (C) Ground-truth Leiden clusters (n=17) for a colorectal cancer whole-slide image dataset. Cells are annotated by Leiden cluster in a 2D UMAP representation of the full biomarker panel (left) and a spatial scatterplot (right). (**D**) Boxplot showing F1-score for the predicted cell type labels at each anchor cell proportion across 1000 random marker panels in the experiment for both the tonsil ROI dataset (orange) and the colorectal cancer WSI dataset (blue). (**E**) Histograms for both the tonsil ROI dataset (orange) and the colorectal cancer WSI dataset (blue) showing the distribution of Pearson correlation coefficients for all 1000 random panels. The correlation coefficient was calculated to test the correlation between anchor cell proportion and F1 score for each panel separately.

Figure 4: COEXIST enables rich spatial profiling of BC TMA cores. (A) Alluvial plot of high-level cell phenotype assignments of the matched cells generated by COEXIST, using either the tumor panel, immune panel, or combined panel for 39 BC subtype TMA cores. **(B)** Alluvial plot of refined cell types for E6 phenotyped with either the immune panel, tumor panel, or combined panel. **(C)** Heatmap of Leiden clusters used to define refined cell types of the matched cells in triple negative BC core E6 based on the combined panel. **(D)** Alluvial plot (top) and biomarker rank plot (bottom) highlighting a subset of tracked cells (n=138) that switched cell type identities between the panels. For the biomarker rank plot, lineage markers were ranked for these 138 cells against the rest of the cells in the core. Purple represents biomarkers derived from the tumor panel, while green represents immune panel biomarkers. **(E)** Visual comparison of the cell phenotypes mapped to their spatial locations in the TNBC core consecutive sections (columns)

before (top row) and after (bottom row) integrating them with COEXIST. **(F)** Recurrent neighborhood analysis heatmap showing cell composition per neighborhood and each neighborhood's frequency in both sections. **(G)** Case study of RCN 7 from **(F)** showing image channels corresponding to RCN 7's markers in both slides (top row) and the presence of RCN 7 after applying COEXIST (bottom row).

Figure 5: **COEXIST provides MTI platform comparisons at the single-cell level.** (**A**) Population-level scatter plot and Pearson's *r* of serial TMA sections with (**A**) all cells and (**B**) shared cells identified with COEXIST. (**C**) Single-cell comparison of mIHC and CyCIF platforms with 10 shared markers, shown with Spearman correlation.

REFERENCES

1. de Souza, N., Zhao, S. & Bodenmiller, B. Multiplex protein imaging in tumour biology. *Nat. Rev. Cancer* **24**, 171–191 (2024).
2. Laberiano-Fernández, C., Hernández-Ruiz, S., Rojas, F. & Parra, E. R. Best Practices for Technical Reproducibility Assessment of Multiplex Immunofluorescence. *Front Mol Biosci* **8**, 660202 (2021).
3. Lin, J.-R. *et al.* Highly multiplexed immunofluorescence imaging of human tissues and tumors using t-CyCIF and conventional optical microscopes. (2018) doi:10.7554/eLife.31657.
4. Guerriero, J. L. *et al.* Qualification of a multiplexed tissue imaging assay and detection of novel patterns of HER2 heterogeneity in breast cancer. *npj Breast Cancer* **10**, 1–22 (2024).
5. Creason, A. L. *et al.* A Web-based Software Resource for Interactive Analysis of Multiplex Tissue Imaging Datasets. *bioRxiv* 2022.08.18.504436 (2022) doi:10.1101/2022.08.18.504436.
6. Du, Z. *et al.* Qualifying antibodies for image-based immune profiling and multiplexed tissue imaging. *Nat. Protoc.* **14**, 2900–2930 (2019).
7. Forjaz, A. *et al.* Three-dimensional assessments are necessary to determine the true, spatially-resolved composition of tissues. *bioRxiv* 2023.12.04.569986 (2024) doi:10.1101/2023.12.04.569986.
8. Multiplexed 3D atlas of state transitions and immune interaction in colorectal cancer. *Cell* **186**, 363–381.e19 (2023).
9. Wang, L., Li, M. & Hwang, T. H. The 3D Revolution in Cancer Discovery. *Cancer Discov.* **14**, 625–629 (2024).
10. Liu, J. T. *et al.* Engineering the future of 3D pathology. *Hip Int.* **10**, e347 (2024).
11. Yapp, C. *et al.* Multiplexed 3D Analysis of Cell Plasticity and Immune Niches in Melanoma. *bioRxiv* 2023.11.10.566670 (2023) doi:10.1101/2023.11.10.566670.

12. Joshi, S. *et al.* Generative interpolation and restoration of images using deep learning for improved 3D tissue mapping. *bioRxiv* 2024.03.07.583909 (2024) doi:10.1101/2024.03.07.583909.
13. Stoeckius, M. *et al.* Simultaneous epitope and transcriptome measurement in single cells. *Nat. Methods* **14**, 865–868 (2017).
14. Haque, A., Engel, J., Teichmann, S. A. & Lönnberg, T. A practical guide to single-cell RNA-sequencing for biomedical research and clinical applications. *Genome Med.* **9**, 75 (2017).
15. Vandereyken, K., Sifrim, A., Thienpont, B. & Voet, T. Methods and applications for single-cell and spatial multi-omics. *Nat. Rev. Genet.* **24**, 494–515 (2023).
16. Lin, J.-R. *et al.* High-plex immunofluorescence imaging and traditional histology of the same tissue section for discovering image-based biomarkers. *Nat Cancer* **4**, 1036–1052 (2023).
17. Tsujikawa, T. *et al.* Quantitative Multiplex Immunohistochemistry Reveals Myeloid-Inflamed Tumor-Immune Complexity Associated with Poor Prognosis. *Cell Rep.* **19**, 203–217 (2017).
18. Burlingame, E. A. *et al.* SHIFT: speedy histological-to-immunofluorescent translation of a tumor signature enabled by deep learning. *Sci. Rep.* **10**, 17507 (2020).
19. Kiemen, A. L. *et al.* CODA: quantitative 3D reconstruction of large tissues at cellular resolution. *Nat. Methods* **19**, 1490–1499 (2022).
20. Burlingame, E. *et al.* 3D multiplexed tissue imaging reconstruction and optimized region of interest (ROI) selection through deep learning model of channels embedding. *Front Bioinform* **3**, 1275402 (2023).
21. Gatenbee, C. D. *et al.* Virtual alignment of pathology image series for multi-gigapixel whole slide images. *Nat. Commun.* **14**, 4502 (2023).
22. Kuett, L. *et al.* Three-dimensional imaging mass cytometry for highly multiplexed molecular and cellular mapping of tissues and the tumor microenvironment. *Nat Cancer* **3**, 122–133 (2022).
23. Liu, Y. *et al.* High-plex protein and whole transcriptome co-mapping at cellular resolution

with spatial CITE-seq. *Nat. Biotechnol.* **41**, 1405–1409 (2023).

24. CosMx SMI Overview - Single-Cell Imaging. *NanoString* https://nanostring.com/products/cosmx-spatial-molecular-imager/single-cell-imaging-overview/ (2021).
25. Guilliams, M. *et al.* Spatial proteogenomics reveals distinct and evolutionarily conserved hepatic macrophage niches. *Cell* **185**, (2022).
26. Sun, C. *et al.* Spatially resolved multi-omics highlights cell-specific metabolic remodeling and interactions in gastric cancer. *Nat. Commun.* **14**, 1–14 (2023).
27. Stanojevic, S., Li, Y., Ristivojevic, A. & Garmire, L. X. Computational Methods for Single-Cell Multi-Omics Integration and Alignment. *Genomics Proteomics Bioinformatics* **20**, 836–849 (2022).
28. Stuart, T. *et al.* Comprehensive Integration of Single-Cell Data. *Cell* **177**, 1888–1902.e21 (2019).
29. Cohen Kalafut, N., Huang, X. & Wang, D. Joint variational autoencoders for multimodal imputation and embedding. *Nature Machine Intelligence* **5**, 631–642 (2023).
30. Dou, J. *et al.* Bi-order multimodal integration of single-cell data. *Genome Biol.* **23**, 112 (2022).
31. Burkard, R., Dell'Amico, M. & Martello, S. *Assignment Problems, Revised Reprint*. (SIAM, 2012).
32. Chen, S., Jiang, S., Ma, Z., Nolan, G. P. & Zhu, B. One-Way Matching of Datasets with Low Rank Signals. (2022).
33. Cao, K., Bai, X., Hong, Y. & Wan, L. Unsupervised topological alignment for single-cell multi-omics integration. *Bioinformatics* **36**, i48–i56 (2020).
34. Zhu, B. *et al.* Robust single-cell matching and multimodal analysis using shared and distinct features. *Nat. Methods* **20**, 304–315 (2023).
35. Chen, S. *et al.* Integration of spatial and single-cell data across modalities with weakly

linked features. *Nat. Biotechnol.* 1–11 (2023).

36. Chang, Y. H. *et al.* Single cell tracking based on Voronoi partition via stable matching. in *2020 59th IEEE Conference on Decision and Control (CDC)* 5086–5091 (IEEE, 2020).
37. Xenium In Situ Platform. *10x Genomics* https://www.10xgenomics.com/platforms/xenium.
38. Crouse, D. On Implementing 2D Rectangular Assignment Algorithms. *IEEE Transactions on Aerospace and Electronic Systems* **52**, 4 (2016).
39. Zhu, J.-Y., Park, T., Isola, P. & Efros, A. A. Unpaired image-to-image translation using cycle-consistent adversarial networks. in *Proceedings of the IEEE international conference on computer vision* 2223–2232 (2017).
40. Burlingame, E. A. *et al.* Toward reproducible, scalable, and robust data analysis across multiplex tissue imaging platforms. *Cell Rep Methods* **1**, (2021).
41. Liu, Y., Beyer, A. & Aebersold, R. On the Dependency of Cellular Protein Levels on mRNA Abundance. *Cell* **165**, 535–550 (2016).
42. Frei, A. P. *et al.* Highly multiplexed simultaneous detection of RNAs and proteins in single cells. *Nat. Methods* **13**, 269–275 (2016).
43. Hussaini, H. M., Seo, B. & Rich, A. M. Immunohistochemistry and Immunofluorescence. *Methods Mol. Biol.* **2588**, 439–450 (2023).
44. Schapiro, D. *et al.* MCMICRO: a scalable, modular image-processing pipeline for multiplexed tissue imaging. *Nat. Methods* **19**, 311–315 (2022).
45. Greenwald, N. F. *et al.* Whole-cell segmentation of tissue images with human-level performance using large-scale data annotation and deep learning. *Nat. Biotechnol.* **40**, 555–565 (2022).
46. Chang, Y. H. *et al.* Deep learning based Nucleus Classification in pancreas histological images. in *2017 39th Annual International Conference of the IEEE Engineering in Medicine and Biology Society (EMBC)* 672–675 (IEEE, 2017).
47. van der Walt, S. *et al.* scikit-image: image processing in Python. *PeerJ* **2**, e453 (2014).

48. RAPIDS. *RAPIDS | GPU Accelerated Data Science* https://rapids.ai.

49. Wolf, F. A., Angerer, P. & Theis, F. J. SCANPY: large-scale single-cell gene expression data analysis. *Genome Biol.* **19**, 15 (2018).

50. Nirmal, A. J. *et al.* The Spatial Landscape of Progression and Immunoediting in Primary Melanoma at Single-Cell Resolution. *Cancer Discov.* **12**, 1518–1541 (2022).

51. Fabian, P. Scikit-learn: Machine learning in Python. *Journal of machine learning research 12* 2825 (2011).

52. Wickham, H. *Ggplot2*. (Springer, New York, NY, 2011).

53. Ggalluvial. http://corybrunson.github.io/ggalluvial/.

54. Ripley, B. D. The R project in statistical computing. *MSOR Connect.* **1**, 23–25 (2001).

55. Waskom, M. seaborn: statistical data visualization. *J. Open Source Softw.* **6**, 3021 (2021).

56. Hunter, J. D. Matplotlib: A 2D Graphics Environment. *Comput. Sci. Eng.* **9**, 90–95 (May-June 2007).

57. Manz, T. *et al.* Viv: multiscale visualization of high-resolution multiplexed bioimaging data on the web. *Nat. Methods* **19**, 515–516 (2022).

58. Keller, M. S. *et al.* Vitessce: integrative visualization of multimodal and spatially-resolved single-cell data. (2021) doi:10.31219/osf.io/y8thv.

FIGURE 1

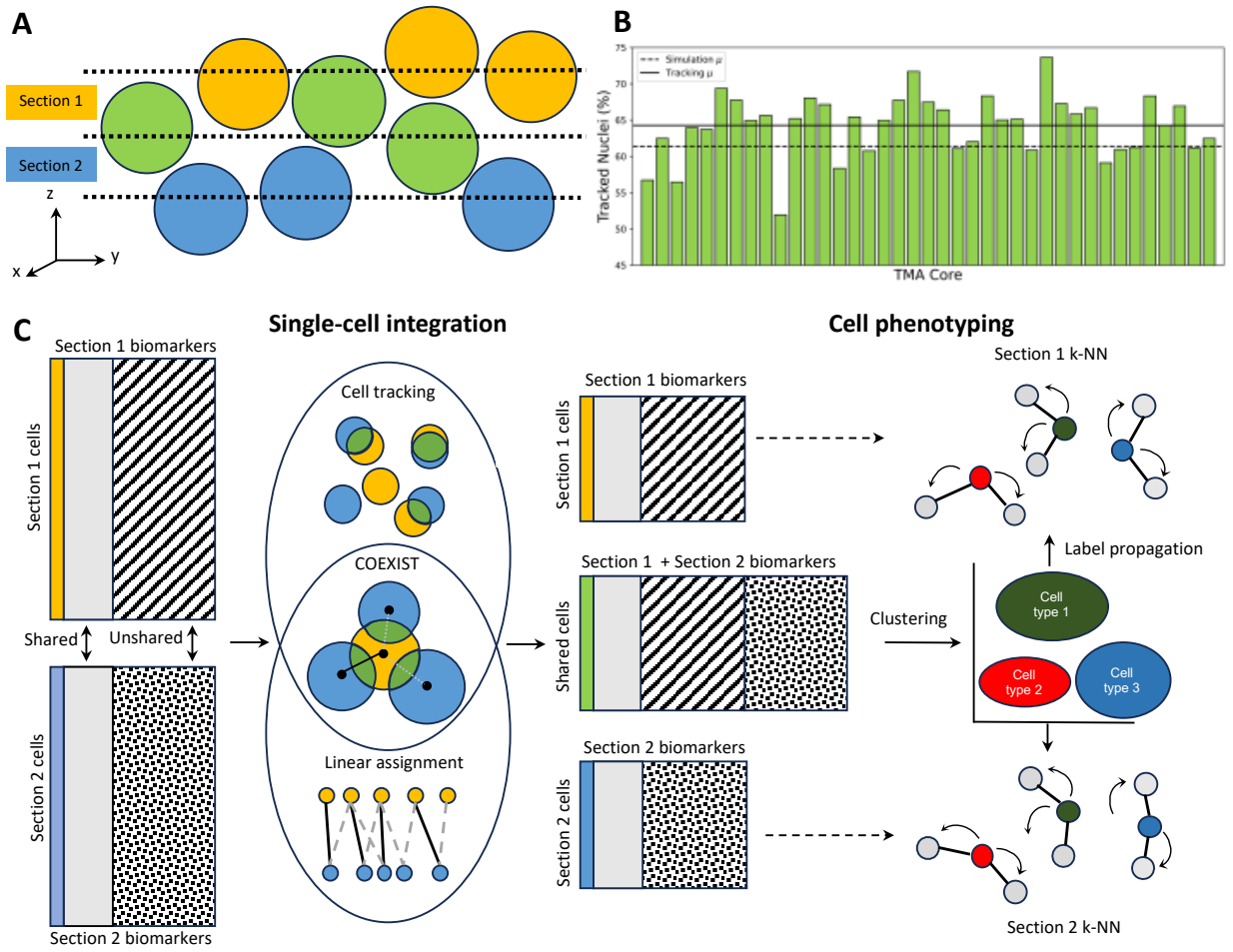
A
Section 1
Section 2
z
y
x
B
Simulation μ
Tracking μ
Tracked Nuclei (%)
TMA Core
C
Single-cell integration
Cell phenotyping
Section 1 biomarkers
Section 1 cells
Shared
Unshared
Section 2 cells
Section 2 biomarkers
Cell tracking
COEXIST
Linear assignment
Section 1 biomarkers
Section 1 cells
Section 1 k-NN
Section 1 + Section 2 biomarkers
Shared cells
Clustering
Label propagation
Cell type 1
Cell type 2
Cell type 3
Section 2 biomarkers
Section 2 cells
Section 2 k-NN

FIGURE 2

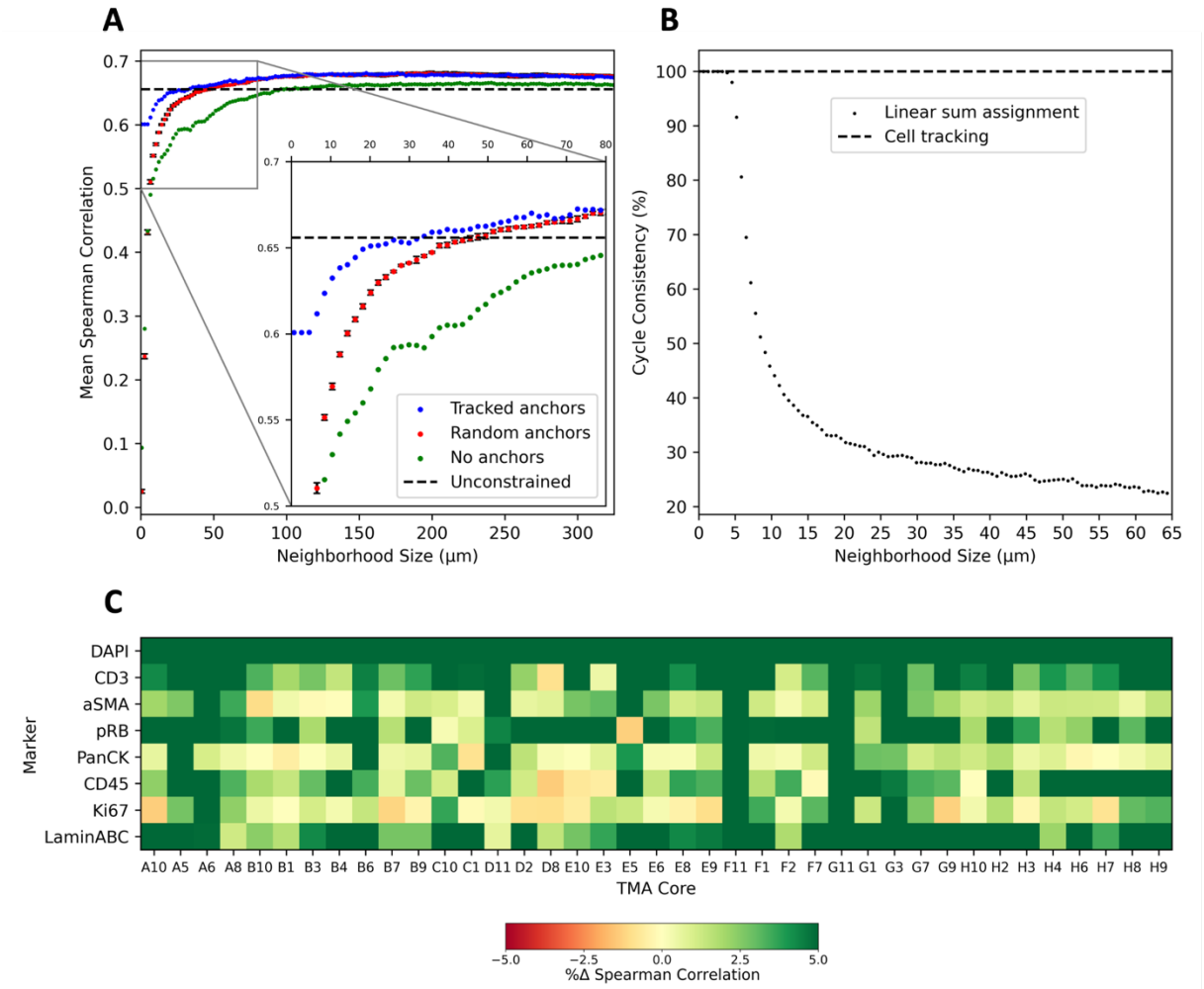
A
Mean Spearman Correlation
Neighborhood Size (μm)
Tracked anchors
Random anchors
No anchors
Unconstrained
B
Cycle Consistency (%)
Neighborhood Size (μm)
Linear sum assignment
Cell tracking
C
Marker
DAPI
CD3
aSMA
pRB
PanCK
CD45
Ki67
LaminABC
A10 A5 A6 A8 B10 B1 B3 B4 B6 B7 B9 C10 C1 D11 D2 D8 E10 E3 E5 E6 E8 E9 F11 F1 F2 F7 G11 G1 G3 G7 G9 H10 H2 H3 H4 H6 H7 H8 H9
TMA Core
%Δ Spearman Correlation

FIGURE 3

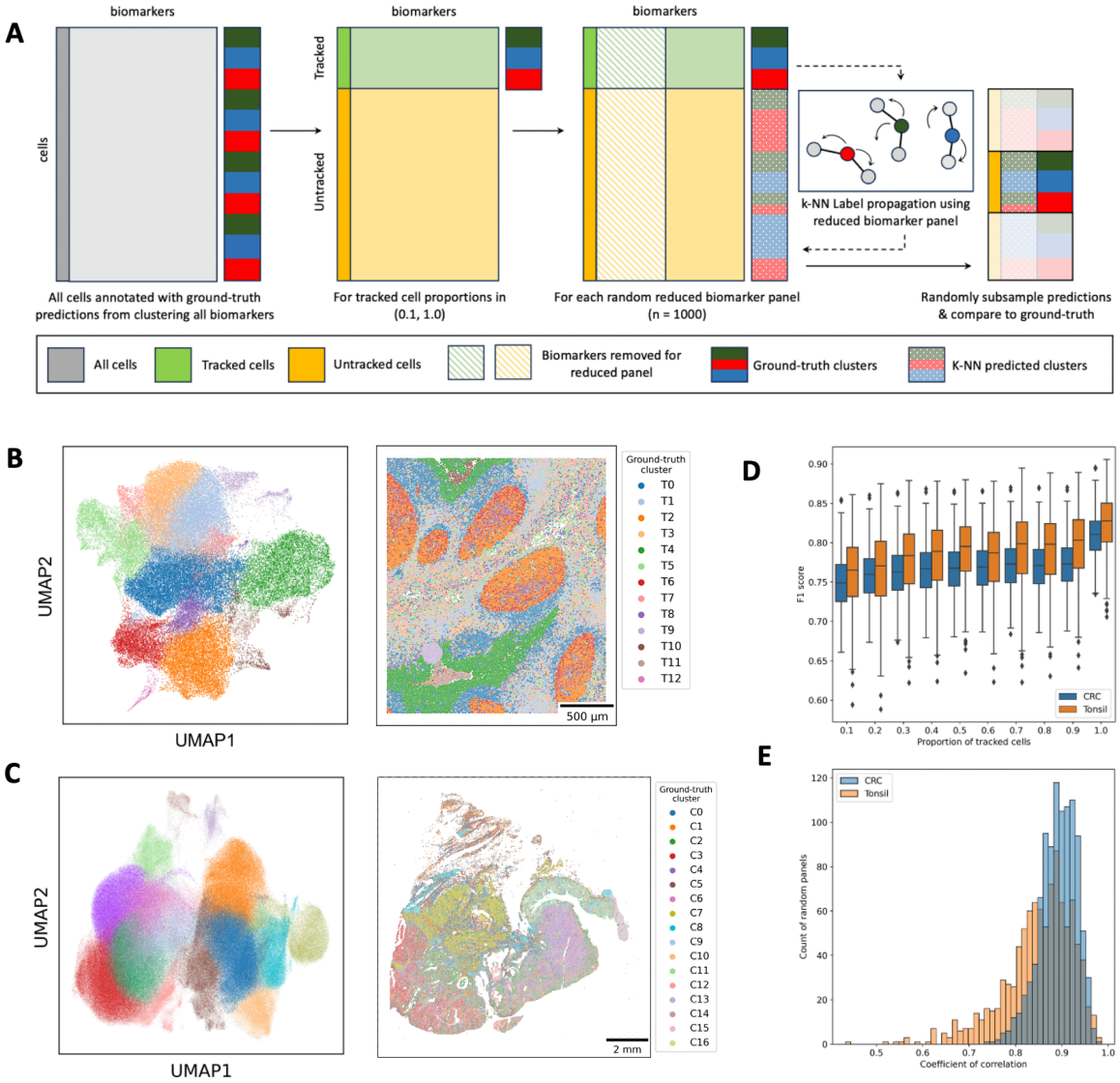
A
biomarkers
cells
Tracked
Untracked
k-NN Label propagation using reduced biomarker panel
All cells annotated with ground-truth predictions from clustering all biomarkers
For tracked cell proportions in (0.1, 1.0)
For each random reduced biomarker panel (n = 1000)
Randomly subsample predictions & compare to ground-truth
All cells
Tracked cells
Untracked cells
Biomarkers removed for reduced panel
Ground-truth clusters
K-NN predicted clusters
B
UMAP2
UMAP1
Ground-truth cluster
T0
T1
T2
T3
T4
T5
T6
T7
T8
T9
T10
T11
T12
500 µm
C
UMAP2
UMAP1
Ground-truth cluster
C0
C1
C2
C3
C4
C5
C6
C7
C8
C9
C10
C11
C12
C13
C14
C15
C16
2 mm
D
F1 score
Proportion of tracked cells
CRC
Tonsil
E
Count of random panels
Coefficient of correlation
CRC
Tonsil

FIGURE 4

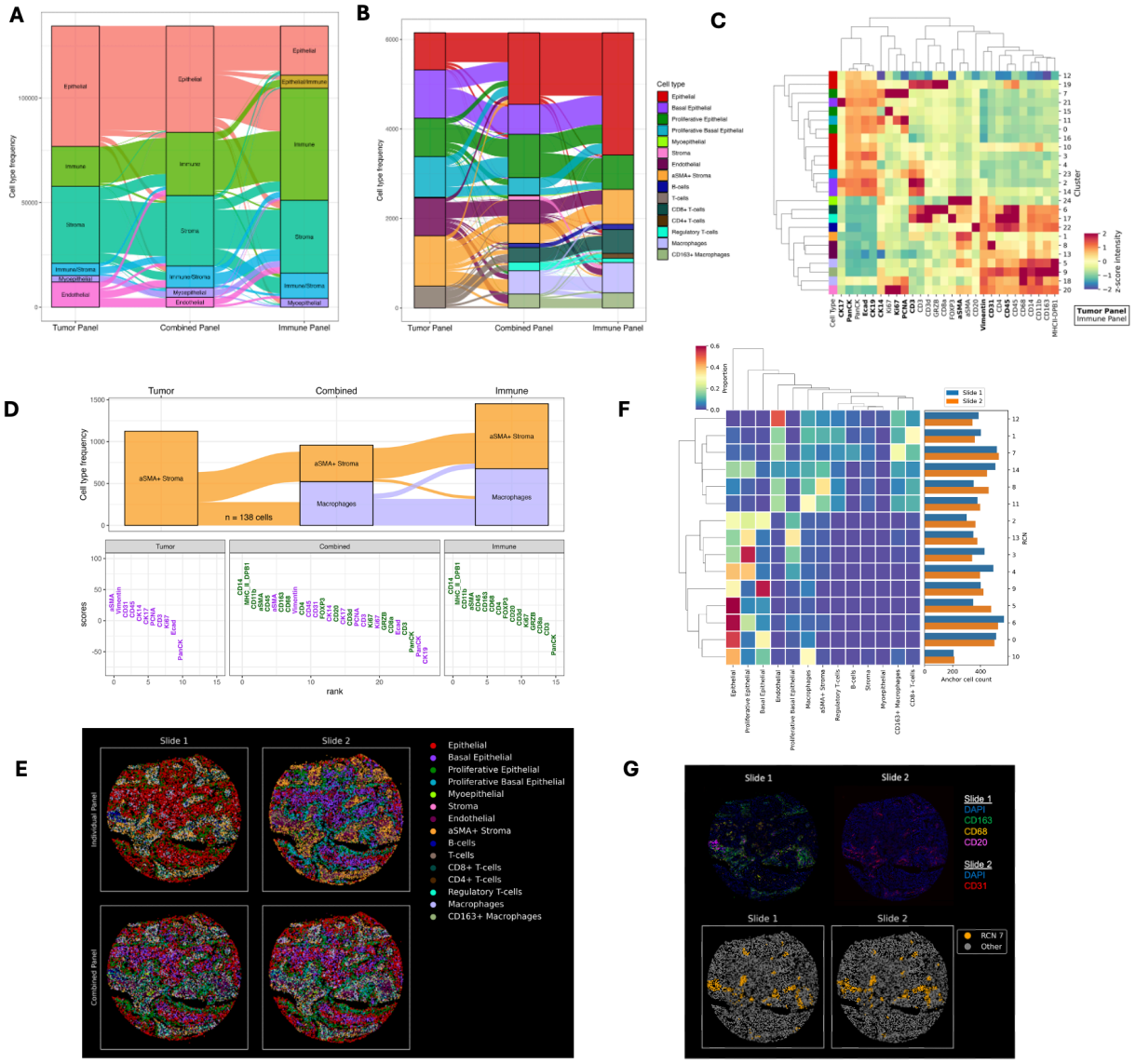
A
Cell type frequency
Tumor Panel
Combined Panel
Immune Panel
B
Cell type
Epithelial
Basal Epithelial
Proliferative Epithelial
Proliferative Basal Epithelial
Myoepithelial
Stroma
Endothelial
aSMA+ Stroma
B-cells
T-cells
CD8+ T-cells
CD4+ T-cells
Regulatory T-cells
Macrophages
CD163+ Macrophages
C
Cluster
z-score intensity
Tumor Panel
Immune Panel
D
Tumor
Combined
Immune
aSMA+ Stroma
Macrophages
n = 138 cells
scores
rank
E
Slide 1
Slide 2
Individual Panel
Combined Panel
F
Proportion
Slide 1
Slide 2
RCN
Anchor cell count
G
Slide 1
Slide 2
DAPI
CD163
CD68
CD20
CD31
RCN 7
Other

FIGURE 5

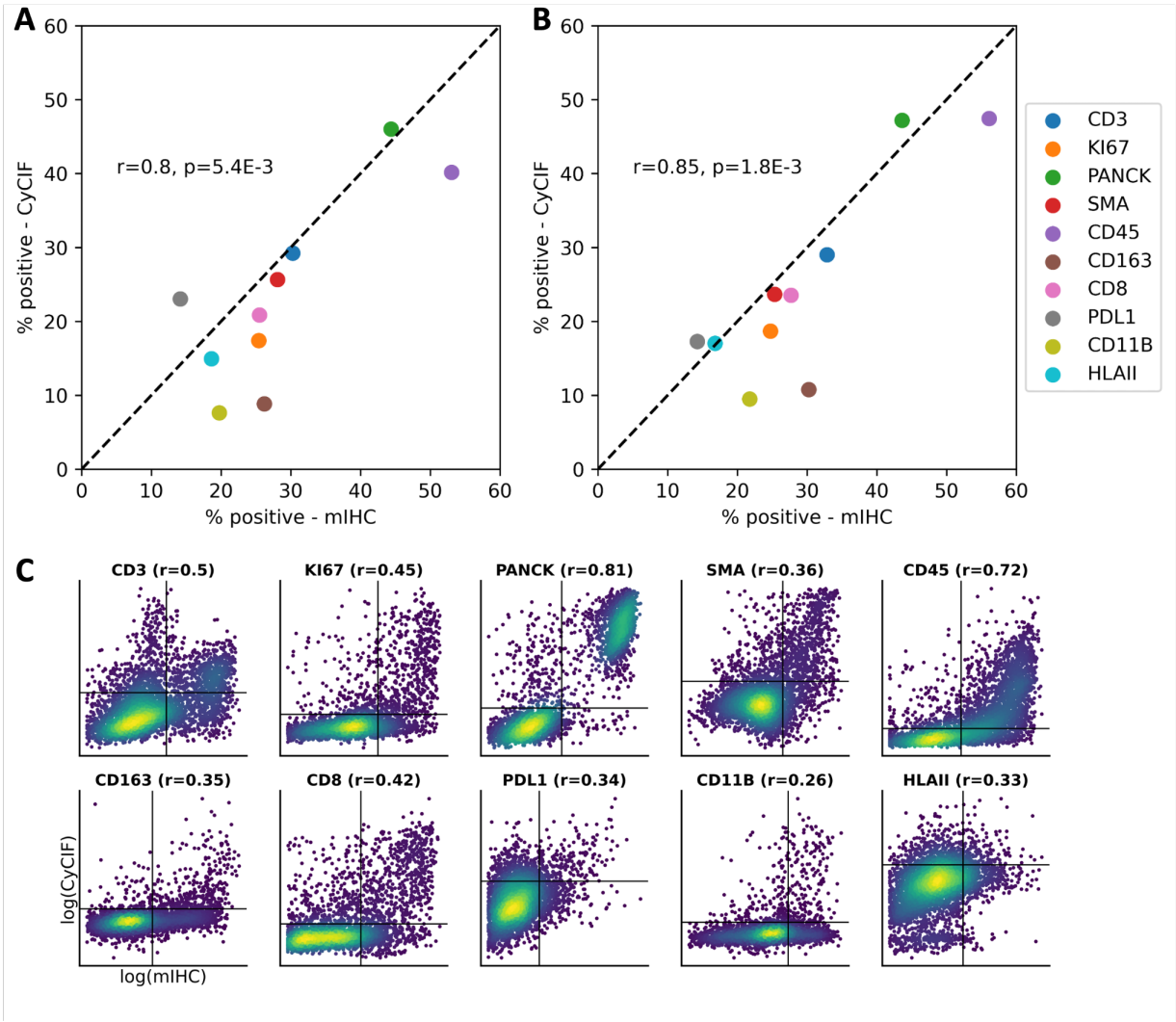
A
B
C
r=0.8, p=5.4E-3
r=0.85, p=1.8E-3
% positive - CyCIF
% positive - mIHC
CD3
KI67
PANCK
SMA
CD45
CD163
CD8
PDL1
CD11B
HLAII
CD3 (r=0.5)
KI67 (r=0.45)
PANCK (r=0.81)
SMA (r=0.36)
CD45 (r=0.72)
CD163 (r=0.35)
CD8 (r=0.42)
PDL1 (r=0.34)
CD11B (r=0.26)
HLAII (r=0.33)
log(CyCIF)
log(mIHC)

SUPPLEMENTARY INFORMATION

Figure S1: Out-of-the-box linear sum assignment does not recover spatial information. (A) y-coordinates of linear sum assignment matches connected by lines across Slide 1 and Slide 2 of core B3 shown on the y-z projection of serial slides. **(B)** y-coordinates of cell tracking matches connected by lines across Slide 1 and Slide 2 of core B3 shown on the y-z projection of serial slides.

Figure S2: Tracked anchors consistently outperform random anchors. Shared marker correlation of cell pairs versus search radius for linear sum assignment matching based on tracked *N* anchors, random *N* anchors, and no anchors for cores H7, F1, H4, G6, E5, and A10.

Figure S3: Mean Spearman correlation of 39 TMA cores for 8 shared markers.

Figure S4: Missing lineage markers in core E06 result in cell identity switching between panels. A subset of tracked cells switched cell type identities between the panels (**Figure 4D**). To investigate this further, we focused on one cell type identity transition. Among the 138 tracked cells, those classified as αSMA+ stroma cells in the tumor panel were reclassified as macrophages on the Immune and Combined panels. The images highlight how these misclassifications can occur. In the immune panel image (right), CD68 (green; canonical macrophage/monocyte biomarker) is clearly abundant and closely co-located with αSMA+ (magenta). As a result, these cells are identified as macrophages in the Immune panel due to the presence of CD68. However, the tumor panel (left) lacks the CD68 marker, leading to their classification as αSMA+ stromal cells. This misclassification may arise from signal spillover from overlapping or nearby stromal cells, or from high autofluorescence in the αSMA channel. By combining the panel, this discrepancy was resolved.

Figure S5: Cell type composition comparison and their transition across panels. Alluvial plot of propagated refined cell types for E6 phenotype with either the immune panel, tumor panel, or combined panel.

Figure S6: Runtime of the COEXIST algorithm with respect to the average number of input cells across consecutive MTIs using core B04 in the TNP-TMA dataset.

Figure S7: Single-cell scatter plots of marker intensity across shared markers in consecutive CyCIF MTIs for core B04.

Table S1: TNP-TMA BC biomarker panels

Figure S1

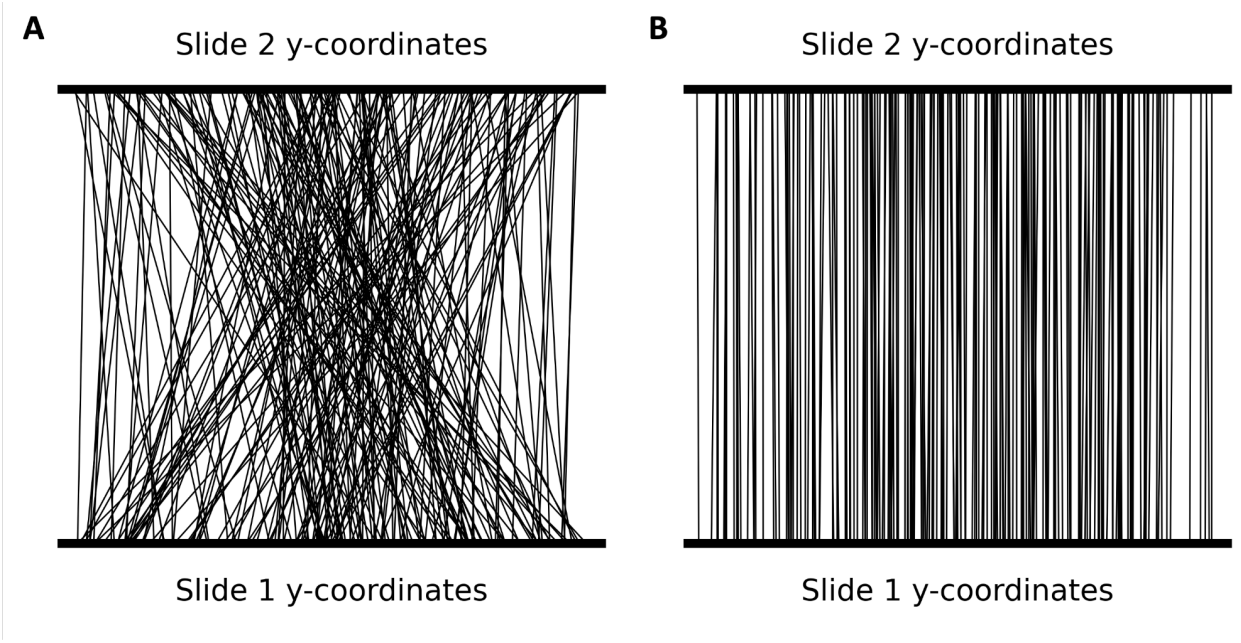
A
Slide 2 y-coordinates
Slide 1 y-coordinates
B
Slide 2 y-coordinates
Slide 1 y-coordinates

Figure S2

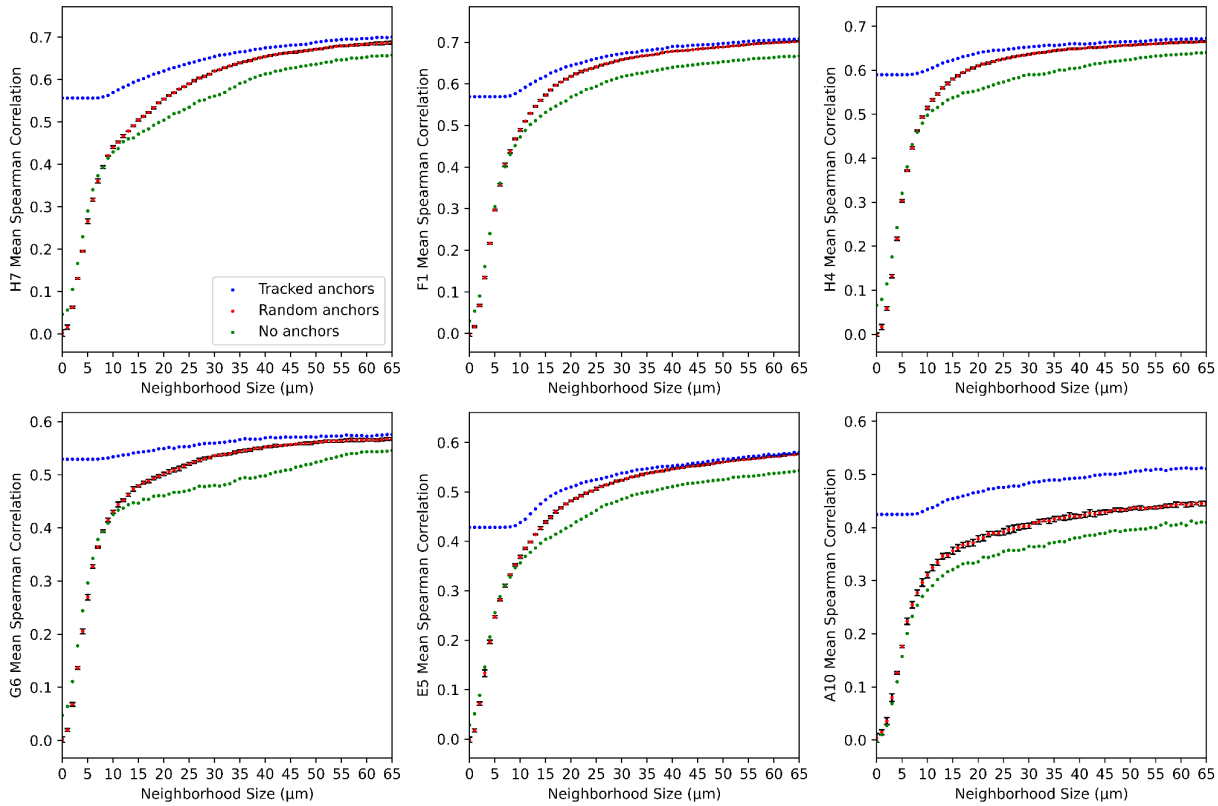
H7 Mean Spearman Correlation
F1 Mean Spearman Correlation
H4 Mean Spearman Correlation
G6 Mean Spearman Correlation
E5 Mean Spearman Correlation
A10 Mean Spearman Correlation
Neighborhood Size (μm)
Tracked anchors
Random anchors
No anchors

Figure S3

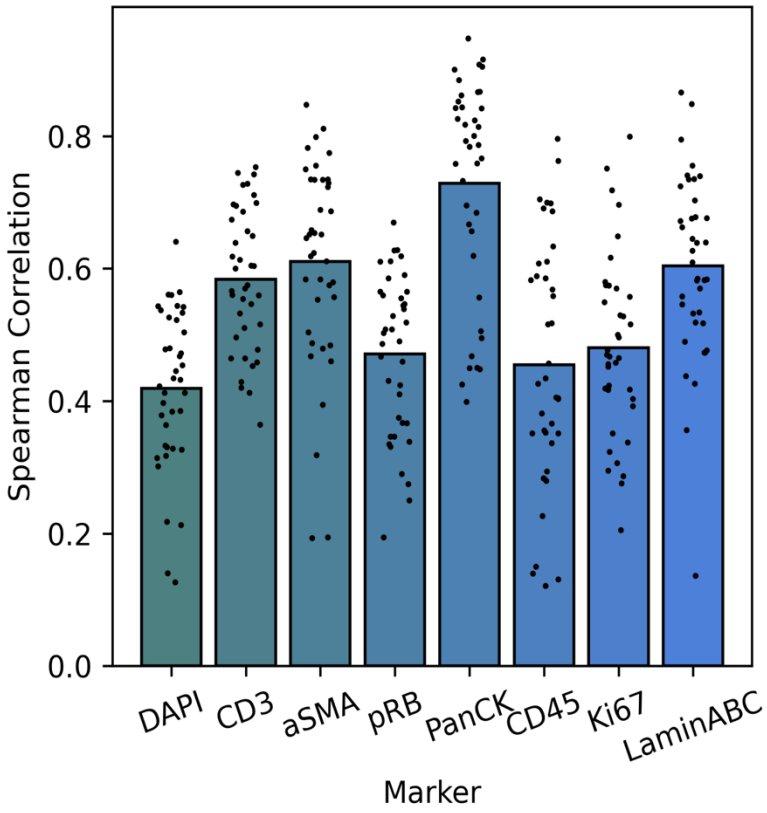
Spearman Correlation
0.0
0.2
0.4
0.6
0.8
DAPI
CD3
aSMA
pRB
PanCK
CD45
Ki67
LaminABC
Marker

Figure S4

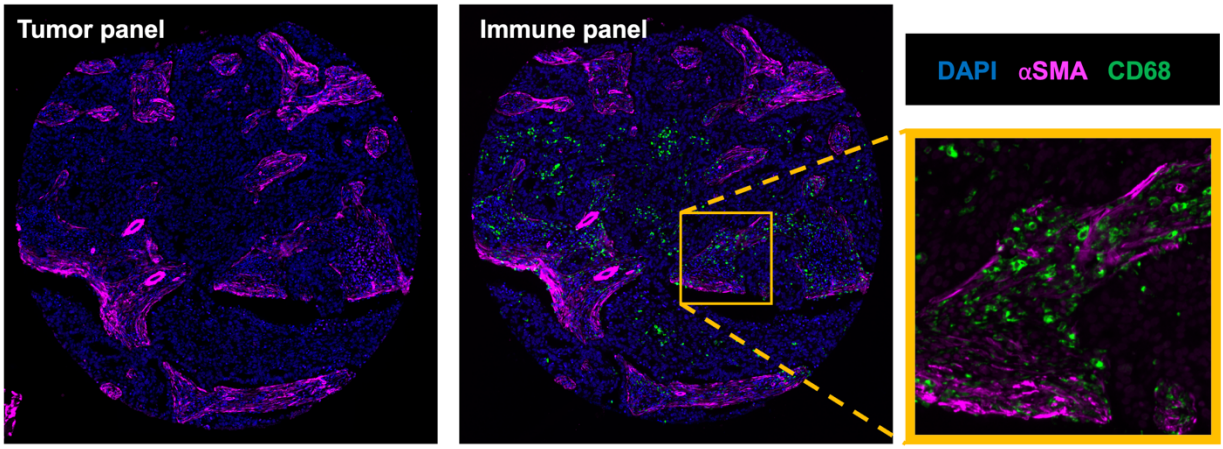

Figure S5

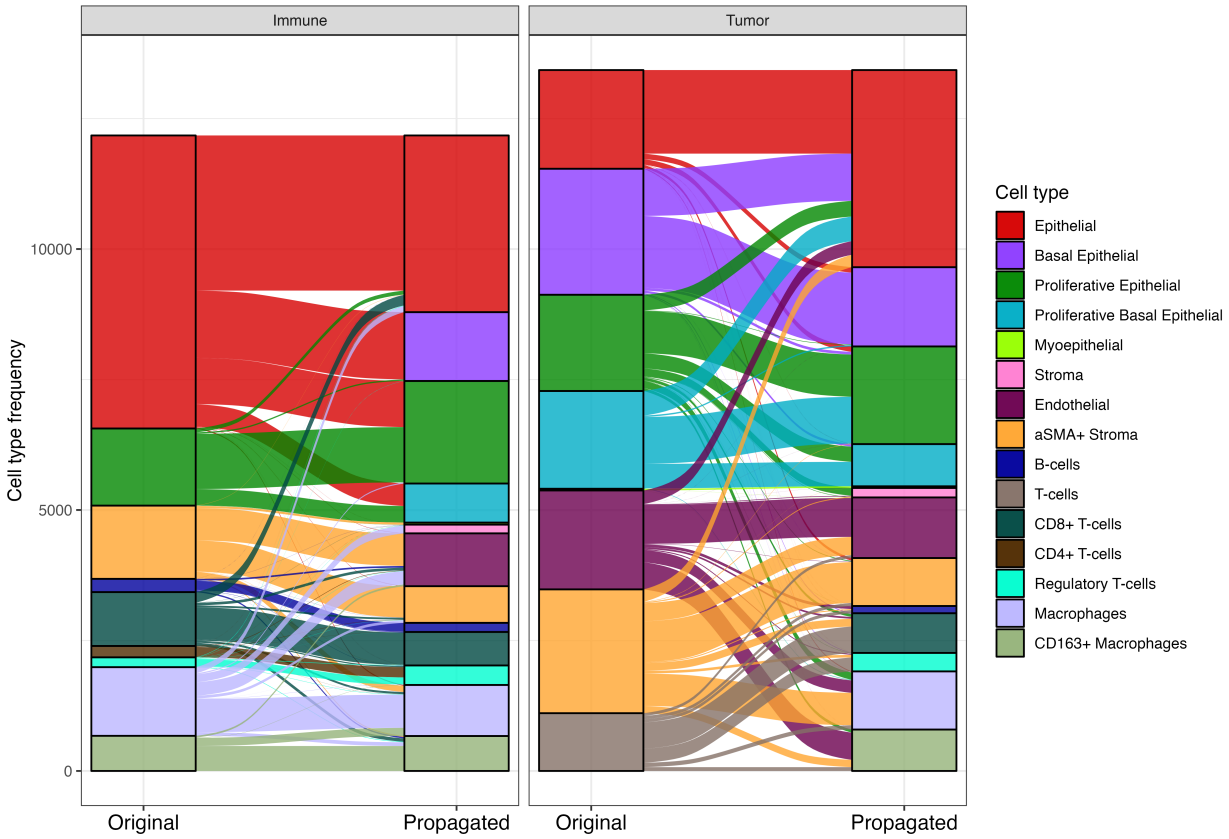
Immune
Tumor
Cell type frequency
10000
5000
0
Original
Propagated
Original
Propagated
Cell type
Epithelial
Basal Epithelial
Proliferative Epithelial
Proliferative Basal Epithelial
Myoepithelial
Stroma
Endothelial
aSMA+ Stroma
B-cells
T-cells
CD8+ T-cells
CD4+ T-cells
Regulatory T-cells
Macrophages
CD163+ Macrophages

Figure S6

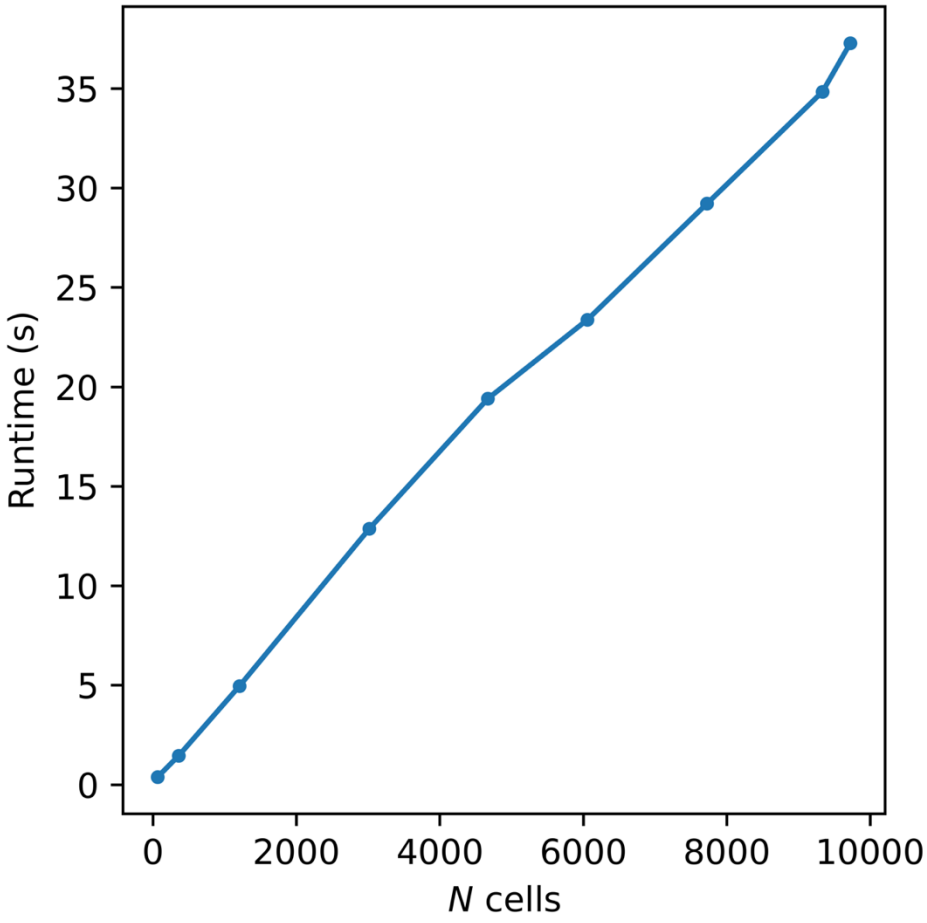
Runtime (s)
0
5
10
15
20
25
30
35
0
2000
4000
6000
8000
10000
N cells

Figure S7

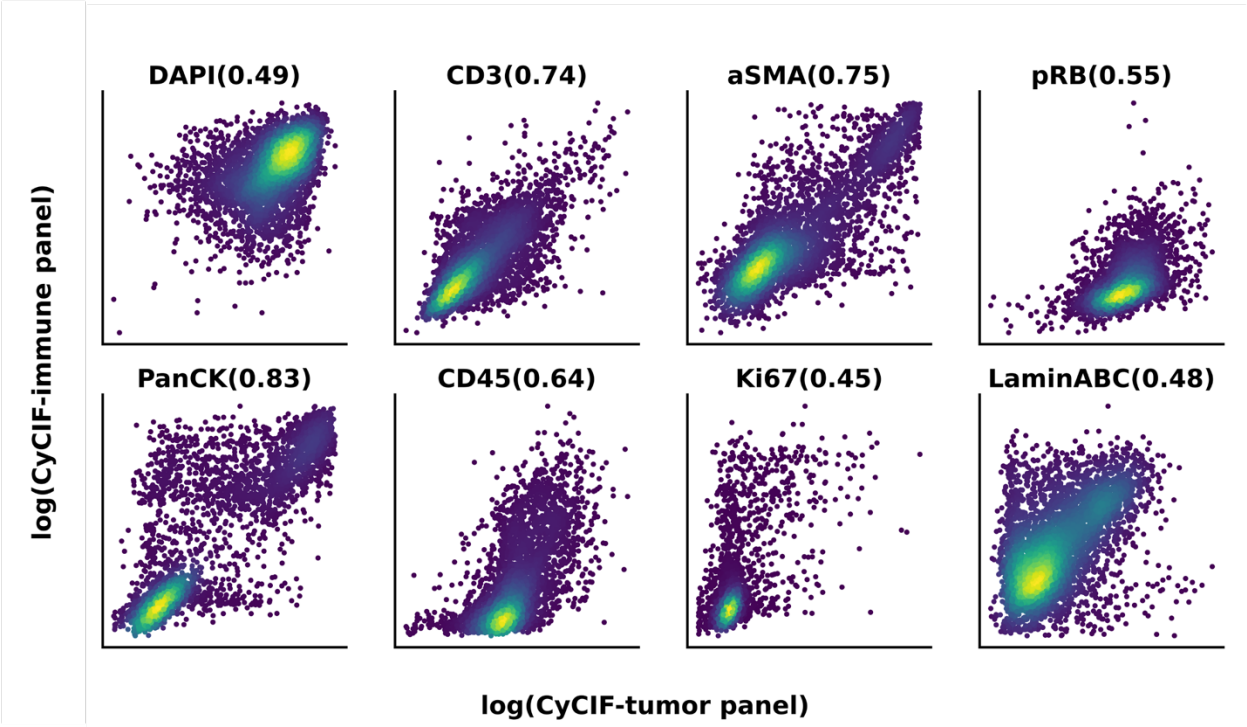
DAPI(0.49)
CD3(0.74)
aSMA(0.75)
pRB(0.55)
PanCK(0.83)
CD45(0.64)
Ki67(0.45)
LaminABC(0.48)
log(CyCIF-immune panel)
log(CyCIF-tumor panel)

Table S1

CyCIF tumor panel	CyCIF immune panel	mIHC panel
DAPI	DAPI	DSDNA
CD3	CD3	CD3
CD45	CD45	CD45
PanCK	PanCK	PanCK
Ki67	Ki67	Ki67
αSMA	αSMA	αSMA
pRB	pRB	TBET
LaminABC	LaminABC	CCR2
ER	GRZB	GRZB
PR	CD8a	CD8
EGFR	CD163	CD163
Vimentin	CD20	CD20
HER2	CD68	CD68
CCND1	PD1	PD1
pERK	FOXP3	FOXP3
p21	PDL1	PDL1
CK14	CD11B	CD11B
CK19	HLA_A	HLAII
CK17	CD4	CD169
Ecad	CD14	CD66B
AR	PDL1_3	DCLAMP
H2Ax	LAG3	CD11C

PCNA	CD3d	EOMES
Rad51	PDL1_2	Hematoxylin
CD31	MHC_II_DPB1	